

Correlation of optical emission and turbulent length scale in a coaxial jet diffusion flame

Shingo Matsuyama *

Aerospace Research and Development Directorate, Japan Aerospace Exploration Agency, Tokyo 182-8522 Japan

Abstract

This article investigates the correlation between optical emission and turbulent length scale in a coaxial jet diffusion flame. To simulate the H₂O emission from an H₂/O₂ diffusion flame, radiative transfer is calculated on flame data obtained by numerical simulation. H₂O emission characteristics are examined for a one-dimensional opposed-flow diffusion flame. The results indicate that H₂O emission intensity is linearly dependent on flame thickness. The simulation of H₂O emission is then extended to an H₂/O₂ turbulent coaxial jet diffusion flame. Time series data for a turbulent diffusion flame are obtained by Large Eddy Simulation, and radiative transfer calculations are conducted on the LES results to simulate H₂O emission optical images. The length scales of visible structures in the simulated emission images are determined by the procedure proposed by Ivancic and Mayer [*J. Propuls. Power* 18 (2002) 247-253]. The length scales of emission intensity are compared with the integral length scales of velocity and temperature evaluated from LES flowfield data. The results clearly indicate that the length scale of emission intensity agrees well with the integral length scale of temperature, and is also close to that of the radial velocity component. Finally, the explanation as to why the integral length scale of temperature can be extracted from emission intensity distributions is stated.

* Address: Aerospace Research and Development Directorate, Japan Aerospace Exploration Agency, 7-44-1 Jindaiji-Higashimachi, Chofu, Tokyo 182-8522, Japan. Fax: +81 422 40 3073.

E-mail address: smatsu@chofu.jaxa.jp

Keywords: H₂O emission; Integral length scale; Turbulent diffusion flame; Large Eddy Simulation; OH* chemiluminescence; Cryogenic rocket combustion

1. Introduction

Measurements of optical emissions from flames are widely conducted in cryogenic rocket engine combustion experiments. UV emissions from the chemiluminescence of electronically excited OH radicals (OH*) are usually recorded by CCD (charge-coupled device) cameras in LOX/H₂ and LOX/CH₄ cryogenic flames [1-8]. The lifetime of OH* is considerably shorter than convection or diffusion times in the combustion chamber. Once excited by chemical reactions, OH* releases a photon and is immediately de-excited, so OH* chemiluminescence emissions are a good tracer of the reaction zone in flames. Several attempts to visualize emissions from combustion products, i.e. H₂O, in the red part of visible spectrum (600-700 nm) have also been made [4,6-8]. These red emissions arise from the vibrational-rotational transitions of thermally excited H₂O, and can be used to indicate regions containing hot products. Comparison of OH* and H₂O emission images show that H₂O emission images give a somewhat thicker distribution.

The emission intensity distribution recorded using a CCD camera is a two-dimensional planar image in which emission intensity is integrated along the lines of sight through the flame. Therefore, for interpreting a local flame structure from the planar images, a deconvolution technique based on the Abel inversion is typically applied. The Abel inversion gives a slice of the mean volumetric OH* emission distribution assuming the flame shape is axisymmetric on average. The line of maximum emission can be traced from a slice obtained via the Abel inversion, which gives the flame expansion angle [2,4-6]. Flame expansion angle is one of few quantitative experimental results available in cryogenic combustion experiments, and the results of numerical simulations of cryogenic

combustion are generally validated by verifying that the flame expansion angle of the simulation reproduces the experimental observation [9-11].

To examine the accuracy of turbulent combustion models for cryogenic combustion, quantitative data which can be used for comparison with simulated results are required over a wide range of operating conditions. Laser diagnostic techniques are usually used to provide such data sets in laboratory scale burners under atmospheric ambient conditions, such as Sandia flames [12]. Recent experiments reported by Singla et al. [13] indicate that planar laser-induced fluorescence (PLIF) of OH radicals is also applicable at high pressures as great as 6.3 MPa. However, OH-PLIF has only recently started to be used in cryogenic combustion, and so far has been applied in extremely high-pressure environments in only a few cases [13-15]. On the other hand, emission images of flame have been used extensively in cryogenic combustion experiments, and a huge database has been accumulated over a wide range of chamber pressures (1 to 100 bar) and injection conditions (various temperatures, momentum flux ratios and injector geometries). The ability to obtain quantitative data from these emission images for simulation validation would be valuable for the development of cryogenic combustion models.

As an attempt to obtain quantitative data other than expansion angle, Ivancic and Mayer estimated length scales from spatially and temporarily resolved OH* emission images using the two point correlation method [7,8]. They assumed that OH* emission structures are determined by the turbulent coherent structures of vortices, and computed length scales using the two-point correlations of OH* emission intensities. The computed length scales were compared with turbulent length scales evaluated by RANS simulation, and the results showed that the experimental length scales lay between the integral and Kolmogorov length scale of RANS simulation, but were closer to the integral length scale. Unfortunately, the reasons why the experimental length scales are close to the integral length scale were not explained further in their study. If turbulent length scales could be

estimated from emission images, the length scale data could also be used to validate Large Eddy Simulation (LES) of cryogenic combustion.

For using the experimental emission length scales to validate the LES results, comparing the experimental and numerical emission length scales would be the most direct route. Such direct comparison of the emission length scales requires detailed modeling of the light emission process by performing radiative transfer calculations for obtaining the emission intensity on the LES. However, this is not practical because radiative transfer calculations in the three-dimensional space of LES are extremely time-consuming to perform solely for the validation. It is more practical to compare the experimental emission length scales with the turbulent length scales such as the integral length scales of velocity components or temperature obtained from the LES flowfield. For meaningful comparison between the experimental emission length scales and the integral length scales in the LES flowfield, a correlation between the emission length scales and the integral length scales must be determined.

In the present study, the correlation between optical emissions and turbulent length scale is investigated for a coaxial jet diffusion flame. The purpose of the present study is to show that the length scales observed in the emission images correspond to the integral length scale of a coaxial jet diffusion flame using the LES flowfield data and the radiative transfer calculations. LES is conducted for an H_2/O_2 coaxial jet diffusion flame under atmospheric pressure to provide turbulent flame data. Radiative transfer is then calculated from the LES flame data, and the emission intensity distribution is obtained numerically, giving a simulated emission image of the flame. The length scale is then estimated from the simulated emission images using the procedure proposed by Ivancic and Mayer [7,8]. This will be compared with integral length scales evaluated directly from the LES flowfield data to examine the validity of estimating length scale from emission images.

2. Numerical methods

2.1 Numerical methods for LES

The governing equations of LES to describe turbulent diffusion flames are three-dimensional filtered compressible Navier-Stokes equations which include the following conservation equations for mass, momentum, energy and species:

$$\frac{\partial \bar{\rho}}{\partial t} + \frac{\partial \bar{\rho} \tilde{u}_i}{\partial x_i} = 0 \quad (1)$$

$$\frac{\partial \bar{\rho} \tilde{u}_i}{\partial t} + \frac{\partial}{\partial x_j} \left(\bar{\rho} \tilde{u}_i \tilde{u}_j + \bar{p} \delta_{ij} - \bar{\tau}_{ij} + \tau_{ij}^{sgs} \right) = 0 \quad (2)$$

$$\frac{\partial \bar{\rho} \tilde{E}}{\partial t} + \frac{\partial}{\partial x_j} \left\{ \left(\bar{\rho} \tilde{E} + \bar{p} \right) \tilde{u}_i + \bar{q}_i - \tilde{u}_j \bar{\tau}_{ij} + H_i^{sgs} + \sigma_i^{sgs} \right\} = 0 \quad (3)$$

$$\frac{\partial \bar{\rho} \tilde{Y}_k}{\partial t} + \frac{\partial}{\partial x_j} \left(\bar{\rho} \tilde{Y}_k \tilde{u}_i + \bar{\rho} \tilde{Y}_k \tilde{V}_{i,k} + Y_{i,k}^{sgs} + \theta_{i,k}^{sgs} \right) = \dot{\omega}_k \left(\bar{\rho}, \tilde{T}, \tilde{Y}_1, \tilde{Y}_2, \dots, \tilde{Y}_{N_s} \right) + \dot{\omega}_k^{sgs} \quad (4)$$

In the present study, all sub-grid terms (τ_{ij}^{sgs} , H_i^{sgs} , σ_i^{sgs} , $Y_{i,k}^{sgs}$, $\theta_{i,k}^{sgs}$, ω_k^{sgs}) in Eqs. (1-4) are neglected and set to zero. As realized in implicit LES (ILES) and Monotone Integrated LES (MILES), numerical dissipation is expected to act like sub-grid terms and emulate the effects of dynamics beyond the grid-scale cut-off.

The governing equations are discretized by a finite volume approach, and the numerical flux is given by the AUSM⁺-up scheme [16] with the fifth-order WENO reconstruction [17]. For reducing the numerical dissipation inherent in the present scheme at low Mach numbers, a simple correction method proposed by Thornber et al. [18] is applied to the reconstructed velocity components. The viscous terms are computed with second-order central difference formulae. Time integration is by the three stage Runge-Kutta method.

Seven chemical species (H_2 , O_2 , OH , H_2O , H , O and HO_2) are assumed and thirteen reactions are considered. The H_2/O_2 reaction mechanism employed in the present study is summarized in Table 1. This mechanism is constructed by eliminating H_2O_2 and chemical reactions involving it from the original reaction mechanism of Li et al. [19] to remove short timescales associated with chemical stiffness. All rate constants of the present reaction mechanism are identical to those in the original mechanism.

Thermodynamic properties are obtained from the NASA Glenn thermodynamic database [20]. The transport properties for pure species are estimated using the CHEMKIN database [21]. Mixture averaged properties for viscosity are obtained by the semi-empirical formula of Wilke [21,22]. For the mixture averaged thermal conductivity, a combination averaging formula by Mathur et al. [21,23] is used. The mixture diffusion coefficients are computed using the method by Bird et al. [21,22].

Computation was carried out using up to 260 processors (1040 cores) of the JAXA Supercomputer System (JSS) installed at the Aerospace Research and Development Directorate (ARD) of the Japan Aerospace Exploration Agency (JAXA). Parallel computation was implemented by domain decomposition, with the Message Passing Interface (MPI) library used for inter-processor communication.

2.2 Numerical methods for radiative transfer calculation

To model the optical emissions from a flame, the radiative transfer equation (RTE) is solved along lines of sight which pass through the flame. The RTE for an emitting, absorbing and non-scattering medium [24] is written as follows:

$$\frac{dI_\lambda}{ds} = -\kappa_\lambda I_\lambda + \kappa_\lambda B_\lambda \quad (5)$$

where I_λ is the spectral radiation intensity, B_λ is the spectral black body intensity (Planck function), s is the direction of radiation propagation, κ_λ is the spectral absorption coefficient of the medium, and the subscript λ denotes wavelength. Integration of Eq. (5) from a point $s' = 0$ to a point $s' = s$ yields

$$I_\lambda(\tau_\lambda) = I_\lambda(0)\exp(-\tau_\lambda) + \int_0^{\tau_\lambda} B_\lambda(\tau'_\lambda)\exp\{-(\tau_\lambda - \tau'_\lambda)\}d\tau'_\lambda \quad (6)$$

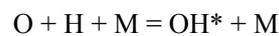
where non-dimensional optical coordinates (optical thickness), τ_λ , is defined as

$$\tau_\lambda = \int_0^s \kappa_\lambda ds \quad (7)$$

The emission intensity from the flame is obtained by integrating Eq. (6) over the wavelength range for which optical measurement is conducted:

$$I = \int_\lambda I_\lambda d\lambda \quad (8)$$

Next, the chemical species which contribute to the optical emissions must be determined. In most optical emission measurements of hydrogen flames, chemiluminescence emissions from OH* are detected. Studies on the chemical kinetics of OH* chemiluminescence [25-29] report that the main source of OH* in H₂/O₂ flame is the reaction



Various rate coefficients of this reaction are reported in [25-29], and the latest work by Kathrotia et al. [29] reports that the highest rate and lowest rate coefficients suggested in the literature differ by two orders of magnitude. It is not clear whether those rate coefficients are also valid in diffusion flames because they are calibrated against shock tube experiments of ignition delay for diluted H₂/O₂ mixtures or hydrogen premixed flames. For these reasons, it seems difficult to model OH* emissions accurately in LES of diffusion flames.

In the present study, therefore, optical emissions from H₂O are considered rather than OH* emissions. Emissions from H₂O arise from vibrational-rotational transitions. Because the vibrational and rotational modes of H₂O are thermally excited modes, the population of an excited state can be calculated from the Boltzmann distribution using flowfield data (temperature, pressure and number density of H₂O) obtained from LES. The evaluation of absorption coefficients is also important to model flame optical emissions accurately. To model the non-gray nature of the absorption of thermal radiation in combustion gases, the absorption coefficients of H₂O are computed by the line-by-line calculation using the HITEMP 2010 database [30]. The vibrational-rotational bands of H₂O exist from the visible to infrared region (600 nm – 10 μm) and about 77 million transitions are included in the HITEMP 2010 database for this wavelength range. Figure 1 shows an example of the absorption coefficients of H₂O computed for typical flame properties of an H₂/O₂ diffusion flame (T=3040K, P=100kPa, 55.84% H₂O by mole). Most spectral lines have absorption coefficients of around 10⁰ m⁻¹ or less, and only a small fraction of lines have coefficients of about 10¹ m⁻¹. The absorption of thermal radiation in the flame is affected by the optical thickness of the gas medium (Eq. (7)), which depends on the physical thickness of the flame. Because the IR emissions of H₂O arise mainly from the high-temperature gas in the diffusion flame, thermal thickness is appropriate for evaluating the optical thickness of the flame. Here, thermal thickness is evaluated as the distance between two points on the one-dimensional flame profile at which the local temperature approaches 1000 K. The

thermal thickness of a H₂/O₂ diffusion flame under the atmospheric pressure condition considered in the present study is of the order of 10⁻³ m (see, for example, Figs. 4 and 7 in Results and discussion), and the optical thickness of the gas medium in the flame is estimated to be less than 10⁻². Thus, the gases in an H₂/O₂ diffusion flame under atmospheric pressure are expected to be optically thin, and light should pass through the flame without being absorbed.

3. Numerical simulation setup

In this article, an LES and a radiative transfer calculation are conducted for a cylindrical combustor equipped with a single shear coaxial injector element. The configurations of the combustor and shear coaxial injector element are shown in Fig. 2. The diameter and length of combustor are 100 and 500 mm, respectively. The combustor has an injector at the upstream end of the combustion chamber. The downstream end of combustion chamber is open and is connected to a sufficiently large buffer zone. The injector element is installed at the center of the combustion chamber. The shear coaxial injector is the most common element type used for oxygen/hydrogen injectors in cryogenic rocket engine combustors. Oxygen is usually injected by the central jet while hydrogen is introduced through the outer annulus. The inner diameter of the O₂ tube (D_i) is 4.9 mm, the outer diameter of the H₂ annulus (D_o) is 7.9 mm and the thickness of O₂ injector lip (T_p) is 0.5 mm. The injector element has no recess. The H₂ and O₂ injection conditions are summarized in Table 2. In the present simulations, constant mass flow rates and temperatures are imposed at the inlets of the injector element. The mass flow rates of gaseous hydrogen and oxygen at the inlets are set to 0.473 and 2.419 g/s, respectively. The propellant mixture ratio, O/F, is about 5.1. The injection temperature is set to 300 K for both reactants. The velocities at the injector exit estimated from the injection mass flow rates are 270 and 100 m/s for H₂ and O₂, respectively. The pressure at the outer boundary of buffer zone is kept at atmospheric pressure (100 kPa). The walls of the combustion

chamber and injector element are adiabatic no-slip walls. The computational domain is divided into about 260 blocks and the computational mesh has about 55 million grid points ($51 \times 51 \times 81$ points \times 260 blocks). The minimum grid spacing is 50 μm in the vicinity of O_2 injector lip. To resolve shear layers and flames, the majority of the computational mesh elements are concentrated in the wake region of the injector exits.

The setup used for the radiative transfer calculation is shown in Fig.3. Light passing through a flame is approximated by a straight line (ray) perpendicular to the image plane of CCD camera. The refraction of light due to density gradient is ignored in the present study. The size of the image plane is 51.2 mm in width ($X = 0$ to 51.2 mm) and 25.6 mm in height ($Y = -12.8$ to 12.8 mm). The image plane is resolved by 512×256 pixels, giving a resolution of 100 $\mu\text{m}/\text{pixel}$ in both directions. This resolution is expected to be sufficient to resolve the turbulent integral length scale. The intensity of light detected at each pixel on the image plane of camera is computed by solving the RTE along the corresponding ray. Light entering each pixel is modeled by a single ray, giving a total of 512×256 rays.

4. Results and discussion

4.1 Optical emissions from a one-dimensional opposed-flow diffusion flame

The first part of the results presented here examines the characteristics of H_2O emissions from a one-dimensional opposed-flow H_2/O_2 diffusion flame. Calculations of the opposed-flow flame are performed using the OPPDIF package of the CHEMKINTM software suite [31]. The chemical reaction mechanism, thermodynamic and transport properties used in the one-dimensional flame calculations are the same models as those used in the LES presented in the next subsection. For the injection conditions of H_2 and O_2 , the temperature and pressure are fixed at 300 K and 100 kPa, respectively. The injection velocities and the distance between $\text{H}_2\text{-O}_2$ inlets are varied to change the

global strain rate on the flame, a , which is defined as

$$a = \frac{|U_{H_2}| + |U_{O_2}|}{L} \quad (9)$$

where U_{H_2} and U_{O_2} are the injection velocities of H_2 and O_2 , respectively, and L is the distance between the inlets.

Figure 4 shows the computed one-dimensional profiles of temperature and number density of H_2O . The fuel boundary is on the positive side and the oxidizer boundary is on the negative side of the one-dimensional ordinate. Results are shown for $a = 280, 820, 2327, 7000$ and 18705 s^{-1} . As the strain rate increases, the flame thickness decreases inversely both in temperature and H_2O number density. Many studies on opposed-flow diffusion flames have reported that flame thickness varies inversely with the square root of the strain rate [32-34]. The flame thickness in the present results also follows this trend. The maximum temperature of flame remains almost constant for $a < 2327 \text{ s}^{-1}$ and is close to the adiabatic flame temperature, then decreases for $a > 7000 \text{ s}^{-1}$ as the extinction limit is approached. Note that the extinction limit of the H_2/O_2 diffusion flame computed with the present chemistry and transport models is more than 10^5 s^{-1} . The strain rate of $18,705 \text{ s}^{-1}$ is still one order of magnitude less than the extinction limit. The peak value of H_2O number density shows the opposite trend to maximum temperature; it increases slightly as the strain rate increases because the density in the flame increases due to the reduction in flame temperature at higher strain rates. The total number density of H_2O integrated over the flame also decreases when the flame becomes thinner (as the strain rate increases), which affects the amount of optical emissions from flame.

To compute the H_2O emission, the RTE is solved along the one-dimensional flame profile. The computed emission intensities as a function of inverse of flame thickness are shown in Fig. 5. Emission intensities are obtained by integrating the spectral intensities for a given wavelength range.

The flame thickness, δ_{flame} , is taken to be the full width at half maximum (FWHM) of the computed temperature profiles. To clarify the dependence on the wavelength range over which spectral intensities are integrated, the H₂O emission is computed for six separate wavelength ranges. These wavelength ranges are resolved by 10^4 wavelength points. The global trend shows that the emission intensity decreases in every wavelength range when the flame thickness decreases (as the strain rate increases). The dependence of intensity on flame thickness changes at around $\delta_{flame} = 1$ mm. The emission intensity decreases linearly with flame thickness at $\delta_{flame} > 1$ mm (low strain rate condition). This linear dependence can be explained by the behavior of temperature and H₂O number density profiles with increasing strain rate, which are shown in Fig. 4. Under low strain rate conditions, the maximum temperature and the peak value of H₂O number density remain almost constant but the flame thickness decreases as the strain rate increases, which means that only the total number of H₂O integrations over the flame decreases. Therefore, emission intensity decreases linearly as the flame becomes thinner. At $\delta_{flame} < 1$ mm (high strain rate condition), emission intensity decreases progressively, although linear dependence is maintained near the extinction limit for $\lambda > 4 \mu\text{m}$. Because optical emissions at shorter wavelength ranges arise from the high-temperature gas medium within the flame, the emission intensities at shorter wavelength ranges decrease when the flame temperature decreases towards the extinction limit. Thus, the emission intensity for $\lambda < 4 \mu\text{m}$ decreases rapidly at $\delta_{flame} < 1$ mm compared with longer wavelength ranges.

The emission intensity results in Fig. 5 are computed with 10^4 wavelength points. The effect of wavelength resolution on emission intensity must be examined because an erroneous line shape given by too low a resolution will affect the absorption and emission by individual spectral lines. It will be assumed that the spectral line shape is approximated by a Gaussian profile, which is

characterized by Doppler broadening. The FWHM of Doppler broadening, $\Delta\lambda_D$, is given as

$$\Delta\lambda_D = \frac{\lambda_c}{c_0} \sqrt{\frac{8kT \ln 2}{m}} \quad (10)$$

where λ_c [μm] denotes the line central wavelength, c_0 [m/s] denotes speed of light in vacuum, k denotes Boltzmann's constant ($=1.3806503 \times 10^{-23}$ J/K), T [K] denotes temperature, and m [kg] denotes the mass of molecules. The FWHM of Doppler broadening estimated with a typical flame property ($T = 3000$ K, $\lambda_c = 1 \mu\text{m}$) is about $10^{-5} \mu\text{m}$. To resolve this small region by 10 wavelength points, the required resolution is $10^{-6} \mu\text{m}$. Thus, to resolve the line shape accurately, about 10^6 wavelength points are required for the computation with a wavelength range of $1 \mu\text{m}$. To reduce the computing time to solve the RTEs, the number of wavelength points should be as low as possible. To examine the error due to too low a wavelength resolution, calculations are conducted for $a = 280 \text{ s}^{-1}$ varying the number of wavelength points from 10^2 to 10^6 . Figure 6 shows the results of computation with different numbers of wavelength points. The computed intensity for each number of wavelength points is normalized by that with 10^6 wavelength points (the most accurate solution). It is surprising that the obtained intensity with 10^4 wavelength points gives a sufficiently accurate solution with errors less of than several percent, and even 10^2 points gives errors of less than 20 percent. Of course, computation with 10^4 wavelength points does not resolve line shape accurately, but the reason why 10^4 wavelength points are sufficiently accurate can be explained by the optically thin condition of the present flame. Under optically thin conditions, absorption by individual spectral lines is not significant and errors in resolving spectral line shape have minimal effect on the integrated emission intensity solutions. Therefore, computation with 10^4 wavelength points is a good trade-off between accuracy and computational cost.

4.2 LES of H_2/O_2 coaxial jet flame

An LES is now conducted to provide time series data for a turbulent diffusion flame. The simulations are initialized by filling the combustion chamber and buffer zone with quiescent H_2 at 300 K. Ignition is achieved by putting high-temperature combustion products (10% OH and 90% H_2O by mass, at 3000 K) in a small region just behind the O_2 injector lip. After the reactants are injected into the combustion chamber and the flame is successfully anchored, no artificial heat source for flame holding is added during the computation. Computation is then conducted for about 50 ms after ignition.

Figure 7 shows instantaneous contours of temperature and vorticity magnitude in the $X - Y$ plane ($Z = 0$ mm) at $t = 40$ ms. The instantaneous temperature field in Fig. 7a shows the flame structures in the near-injector region. The flame is always anchored at the O_2 injector lip, and an H_2/O_2 diffusion flame can be observed in the present result. The observed maximum flame temperature is about 3,300 K, which does not greatly differ from the adiabatic flame temperature of a stoichiometric mixture of H_2/O_2 at atmospheric pressure. Instantaneous contours of vorticity magnitude in Fig. 7b show the development of the shear layers obtained in the present simulation. Two shear layers are clearly observed in vorticity field. The inner one is formed between the O_2 jet and the high speed annular H_2 jet, and the outer one is formed at the outer edge of the annular H_2 jet. Because no velocity fluctuation is added at the inlets in the present simulation, these two shear layers are almost laminar in the vicinity of the injector exit. As the shear layers are convected to downstream locations, coherent vortices are generated and vortex-pairings arise at around $X = 5$ mm. After the pairings arise, the shear layers tends to be turbulent at around $X = 10$ mm, and the inner and outer shear layers merge at a further downstream location. The flame surface on the O_2 jet side is smooth but that on the H_2 jet side exhibits a small scale wrinkled structure due to interaction with coherent vortices produced by the turbulent annular H_2 jet.

Figure 8 shows the three-dimensional structures of the flame and vortices. Figure 8a shows three-dimensional structure of the flame by the iso-surface of temperature ($=1,000$ K). For $X < 10$ mm the flame has a smooth surface because flow is almost laminar in the vicinity of the injector exit, but a highly wrinkled surface is observed for $X > 10$ mm due to interactions with vortices. Figure 8b shows iso-surfaces of the second invariant of the velocity gradient tensor ($Q=2(U_{H2}/D_o)^2$) colored by streamwise vorticity ($-2(U_{H2}/D_o) < \omega_x < 2(U_{H2}/D_o)$). As shown in the instantaneous vorticity field of Fig. 7b, the shear layer is almost laminar in the vicinity of the injector exit and axisymmetric vortex rings are generated first. After pairings occur, the shear layer tends to become turbulent, and then smaller three-dimensional structures can be observed from $X = 10$ mm.

To examine the quality of the computational mesh used in the present LES, the resolved kinetic energy spectrum are evaluated. Figure 9a shows the power spectrum of radial velocity fluctuations. The probe locations at which time series data are collected are also shown in Fig. 9b. As shown in the figure, the Kolmogorov $f^{-5/3}$ spectrum is recovered by the present LES, indicating that the resolution of the employed computational mesh is acceptable. Note that time series data are collected at $5 \mu\text{s}$ intervals in the present simulation, and therefore the power spectrum is obtained only up to 100 kHz.

For further validating the accuracy of the present LES, the stoichiometric mixing length is compared with the experimental data of Shumaker and Driscoll [35]. Figure 10 shows the result of comparison between the present LES and the experimental data. The stoichiometric mixing length (L_s) measured in the experiment is scaled according to the following relationship:

$$\frac{L_s}{D_i} = C \left(M_{eff}^{1/2} X_s \right)^{-1} \quad (11)$$

where C denotes a scaling constant, X_s denotes the mole fraction of inner jet fluid in a stoichiometric

mixture (=0.34 for H₂/O₂ flame), and the effective momentum flux ratio, M_{eff} , is defined as follows:

$$M_{eff} = \frac{(\rho_{H_2})_{eff} U_{H_2}^2}{\rho_{O_2} U_{O_2}^2} \quad (12)$$

where the effective density of outer jet fluid $(\rho_{H_2})_{eff}$ is calculated from the equivalence principle of Tacina and Dahm [36,37]. The stoichiometric mixing length in the present LES is defined as the distance between the nozzle exit and the position where stoichiometric conditions occur along the centerline (see also [35] for the definition of L_s). The values of L_s are normalized against D_i and plotted against the scaling parameter $(M_{eff}^{1/2} X_s)^{-1}$. The dashed line in the figure represents the scaling law for coaxial jet flames derived in [35]. In the present study, a LES is performed with no sub-grid terms under a high Reynolds number. To assess the effect of neglecting the sub-grid terms on the computed flowfield results, additional simulations are performed with a coarse mesh in which grid spacing is doubled from the baseline mesh (55 million grid points) in all directions. Thus, the resulting coarse mesh has about 7 million grid points ($26 \times 26 \times 41$ points \times 260 blocks). In the present LES using the baseline mesh, no velocity fluctuations are added to the inlet velocity conditions, which would also influence the results under high Reynolds number condition to some extent. These additional simulations using the coarse mesh are, therefore, performed with and without velocity fluctuations at the inlets for assessing the influence of the velocity fluctuations. The magnitude of the velocity fluctuations is set to 5% of the average velocity value. The present LESs are performed using the baseline mesh (baseline) and the coarse mesh (coarse), and inlet velocity fluctuations are added to the inlet velocity in the case of the coarse mesh (coarse + v'). The comparison of L_s with the experimental data shows that all three computations agree well with the experimentally derived scaling relation, and the observed errors from the experimental data are approximately 10%. Although the two additional computations using the coarse mesh give slightly

shorter L_s , the differences between the computed L_s values using the baseline mesh and the coarse mesh are smaller than 20%. The comparison between the computations using the coarse mesh with and without velocity fluctuations shows that the influence of the velocity fluctuations on L_s is negligible. The flowfield result obtained using the baseline grid without velocity fluctuations at the inlets is, therefore, sufficiently accurate and worth being analyzed in detail.

The integral length scales are determined by the two-point correlation of velocity and temperature obtained from the present LES. The correlation function at a certain axial location, X , takes the form

$$K(\Delta X) = \frac{\overline{q'(X) \cdot q'(X + \Delta X)}}{q'(X)^2} \quad (13)$$

where the over bar denotes time averaging, q corresponds to velocity components or temperature, and ΔX is the spatial increment in the axial direction. Spatial correlations are computed only in the axial direction in the present study. Time averaging is conducted on time series data of 1,000 points sampled over 5 ms. The integral length scales in the present simulation are defined as the distance at which the value of correlation function reaches 0.5. This definition of length scale is consistent with the procedure in the experiment by Ivancic and Mayer [7,8]. The length scale defined by this procedure is sufficiently accurate, and the difference between the obtained length scale and that defined by the usual definition (area under the curve) is very small, as stated in [7,8]. Furthermore, the cost of computing the exact integral length scale can be reduced drastically by this procedure. Of course, there is no restriction on computing the integral length scale according to the usual definition. The correlation functions are computed along the line of maximum velocity of the turbulent annular H_2 jet, which corresponds to the centerline of the annular jet. Because the flame surface is wrinkled mainly by vortices from the turbulent annular H_2 jet in the present H_2/O_2 coaxial jet setup (see Fig.

7), the length scales of H₂O emissions are expected to be correlated with the turbulent length scales of the H₂ annular jet. Therefore, the integral length scales of the annular H₂ jet should be evaluated. The radial position of the line of maximum velocity of the present LES, r_c , is fitted by the following function of X :

$$r_c(X) = 0.075X + 3.25 \quad (14)$$

where r_c and X are in [mm]. The correlation functions at X (and r_c) are computed at 200 circumferential locations (at 1.8 degree intervals) and averaged circumferentially. The radial location of the line of maximum velocity is shown in Fig. 11 with the time averaged axial velocity field.

Figure 12a shows the integral length scales obtained from the present LES using the baseline mesh. The solid lines show the results obtained with the spatial increment in the $+\Delta X$ direction, and the dashed lines show those with the spatial increment in $-\Delta X$ direction. The two different increment directions give almost the same results. The integral length scales are obtained only for $X > 10$ mm because the flow is almost laminar in the vicinity of the injector exit. The integral length scales obtained from radial, circumferential and axial velocity components (U_r , U_θ , U_X) show that the integral length scale of U_θ is smallest and that of U_X gives the largest scale. The integral length scale of U_r lies between U_θ and U_X but is closer to U_θ . The length scale obtained from temperature is slightly larger than that of U_r . All of the length scales grow from 0.5 to about 2 mm toward the downstream. The minimum grid spacing of the present LES is 50 μm in the vicinity of the injector exit, thus the integral length scales are resolved by at least ten grid points. The integral length scales obtained from the additional simulations using the coarse mesh with and without the inlet velocity fluctuations are shown in Figs. 12b and c. The global trend shows that the integral length scales obtained from the simulations using the coarse mesh exhibit slightly larger scales for

all velocity components and temperature compared with those obtained from the baseline simulation. The addition of velocity fluctuations at the inlets shortened the length scale of U_x , but those of U_r , U_θ and temperature remained unaffected. Although the solutions of the three computations did not converge completely, the differences observed in the obtained integral scales are not significant (<20%). The comparison between the computations with two different grid resolutions shows that the integral length scales are well resolved in the present LES.

4.3 Evaluation of length scale from simulated H₂O emission images

The LES flowfield data is used as a time series data to simulate H₂O emission measurements. The simulated H₂O emission images are then used to determine the emission length scale of emission images. The emission intensity detected by each pixel of a CCD camera is modeled by solving the RTE along the ray which passes through the flame as shown in the numerical setup (see Fig. 3). The H₂O emission images generated using the LES flowfield data at $t=40$ ms are shown in Fig. 13. The results are shown for the same six separate wavelength ranges selected for the one-dimensional opposed-flow diffusion flame of subsection 4.1. To reduce the computing time of the radiative transfer calculation in full three-dimensional space as much as possible, the wavelength ranges are resolved by 10^3 wavelength points. Evaluation of the dependence on wavelength resolution in the one-dimensional flame shows that the magnitude of the error that arises due to calculation with 10^3 points is less than 10%, which is acceptable. The shape of the flame surface which is used for the radiative transfer calculation is also shown by the iso-surfaces of temperature at 1000 and 2500 K in the figure. All of the computations with six wavelength ranges show similar results, but the maximum intensity varies significantly depending on the wavelength range. The emission intensities are strongest for wavelength ranges from 1 to 2 μm and from 2 to 4 μm . This can be explained by the peak wavelength of black body radiation, given by Wien's displacement law [24] as

$$\lambda_{\max} = \frac{2897.8 \mu\text{m} \cdot \text{K}}{T} \quad (15)$$

where λ_{\max} is in [μm]. The estimated peak wavelength is about 1 μm because the typical flame temperature in the present LES is about 3000 K (see Fig. 7). Thus, emission intensities for wavelength ranges around 1 μm are strongest in the present flame. Furthermore, the similarity between the flame shapes in the iso-surface of 2500 K and the emission images is noteworthy. The flame shape is sensitive to the chosen iso-surface value, as shown by the iso-surfaces at two different temperatures. The iso-surface of 1000 K shows smaller-scale structures than the iso-surface of 2500 K, and the pattern observed on the iso-surface of 1000 K is not very similar to the intensity distributions observed in the emission images. Because the peak wavelength of black body radiation at 3000 K is estimated at around 1 μm , most IR emissions of H_2O arise from the high-temperature gas medium within the flame. Thus, the flame shape in the iso-surface of the higher temperature (2500 K) shows better similarity to the emission images, and the highly wrinkled flame surface pattern seems to be duplicated by the intensity distributions in the emission images.

The length scale is now evaluated from the simulated emission images. In the procedure proposed by Ivancic and Mayer [7,8], the visible length scale of emission intensity structure is determined by the two point correlation of intensity signals on two neighboring pixels (pixels 1 and 2) as follows:

$$K_{\text{pixel1}, \text{pixel2}} = \frac{\overline{I'_{\text{pixel1}} \cdot I'_{\text{pixel2}}}}{\sqrt{I'^2_{\text{pixel1}}} \cdot \sqrt{I'^2_{\text{pixel2}}}} \quad \text{with : } I' = \bar{I} - I \quad (16)$$

The computation of the length scale by two point correlation is conducted using the intensities of pixels along the symmetry line because only at these pixels it is ensured that light passes through the

flame perpendicular to the flame surface [7,8]. Note that the line “ $Y = 0$ ” in emission image in Fig. 13 corresponds to the symmetry line. The emission length scales are defined as the distance at which $K_{pixel1,pixel2} = 0.5$. Figure 14 shows examples of correlation functions computed at several axial locations ($X = 20, 30$ and 40mm) for the wavelength range 1 to $2\mu\text{m}$. The spatial correlation distributions become wider as the sampling location moves downstream.

Figure 15 shows the length scales obtained from the simulated emission images. The computed emission length scales are shown for the baseline simulation and the additional simulations using the coarse mesh. The two point correlations are computed using 1,000 single shots of emission images. The length scales of emission intensity give very large scales for $X < 10\text{mm}$ because the flame surface is smooth in this laminar region. The emission length scales for $X > 10\text{mm}$ agree well with the integral length scale of temperature across all three simulations results, and the integral length scales of U_r are close to the emission length scale only for the baseline simulation. The length scales obtained with different wavelength ranges show only small differences, although wavelength ranges from 4 to $6\mu\text{m}$ and from 6 to $8\mu\text{m}$ give slightly larger scales. The emission length scales computed from the simulated emission images with two different grid resolutions produce insignificant differences, indicating that the H_2O emission structures are well resolved in the present LES modeling.

In the present study, the refraction of light due to density gradient is ignored in the radiative transfer calculations. As is the case with laser diagnostics, however, the refraction of light is a potential source of measurement error. Therefore, to assess the effect of refraction on the measurement error, the refraction angles resulting from the density gradient within the present flame are estimated along the rays on the $Y = 0\text{mm}$ plane. The refraction angle, θ , is computed along a ray on the $Y = 0\text{mm}$ plane as follows:

$$\theta = \int_z \left\{ \frac{1}{n} \sqrt{\left(\frac{\partial n}{\partial X} \right)^2 + \left(\frac{\partial n}{\partial Y} \right)^2} \right\} dZ \quad (17)$$

where θ is in [rad], and the refractive index of gas mixture, n , is given as follows:

$$n = 1 + \sum_i \rho_i R_{Gi} \quad (18)$$

where ρ_i [mol/cm³] denotes the molar density, and R_{Gi} [cm³/mol] denotes the molar refractivity of species i . The values of R_{Gi} for each species are taken from [38]. Because the refraction angle is very small (as shown later), the rays along which the refraction of light is computed are assumed to be straight lines. The refraction angles are evaluated using time series data of 1,000 samples of LES flowfield data. Figure 16 shows the computed refraction angles along the rays on the $Y = 0$ mm plane. Instantaneous data are indicated by gray symbols in the scatter plots, and the solid line shows the time-averaged data at each X location. Most instantaneous refraction angles are smaller than 0.05°, and the time-averaged data are very small as well, indicating that the refraction of light is negligible under the present condition.

To support the validity of estimating length scales from emission images, the explanation as to why the integral length scale of temperature can be extracted from emission intensity distributions is further explored. Figure 17 shows the cross section of the instantaneous temperature field at the $Y = 0$ mm plane and the corresponding computed emission intensity distributions. The emission intensity is normalized by its peak value for each wavelength range. Radiative transfer calculations are conducted in the $+Z$ direction from top to bottom of the temperature cross section. The emission intensity distributions show that the intensity is small at the axial position where the flame is thinned by vortices (e.g. at $X = 10$ mm), and vice versa. This dependence of emission intensity on flame thickness is consistent with that observed in a one-dimensional opposed-flow diffusion

flame. Thus, the emission intensity distributions simply correspond to the flame thickness distributions, and the spatial correlation of emission intensity is linked with that of temperature. As a consequence, the length scales extracted from emission images agree well with the integral length scales of temperature. It also should be noted that flame thickness is mainly affected by the velocity fluctuations normal to the flame surface, i.e. by the fluctuation of U_r , thus the length scales of emission images are also close to the integral length scale of U_r .

4.4 Perspective for high-pressure applications in rocket engine combustor

Finally, the effects that are not considered in the present study are examined to give a perspective for future high-pressure applications in the rocket engine combustor. Under high-pressure environments in rocket engine combustors, the refraction of light at the edge of the LOX jet core will be an issue, as pointed out in Refs. [4-6]. In addition, the absorption coefficients of the gas medium increase substantially, and the effects of radiation absorption are not negligible for some wavelength ranges. For example, under 100 atm, the absorption coefficients of H₂O become two orders of magnitude larger than those under 1 atm because the number density increases linearly with pressure. The flame thickness decreases to 1/10 compared with the flame thickness under 1 atm [34]. Therefore, the optical thickness of the flame may approach around 10^{-1} for wavelengths larger than 3 μm , as estimated using the data in Fig. 1. However, the absorption coefficients for wavelengths shorter than 2 μm are two orders of magnitude smaller than those for wavelengths larger than 3 μm . Thus, the medium in the rocket engine combustor is expected to be optically thin condition for wavelengths shorter than 2 μm . The influence of absorption effects for longer wavelengths on the correlation between the emission length scales and the turbulent length scales under high pressures are not clear and need to be investigated in future works on rocket engine applications.

In addition, the selection of a suitable wavelength range for collecting the H₂O emissions would

be important. For effectively detecting the H₂O emission in the diffusion flame, the shorter wavelength range would be better because high-temperature gas (>3000 K) would exist only within the flame. Specifically, wavelengths shorter than 1 μm would be suitable for the rocket engine application. Because the peak wavelength of blackbody radiation at 3000 K (typical adiabatic flame temperature of H₂/O₂ combustion) is approximately 1 μm, H₂O emissions shorter than 1 μm originate only from the high-temperature flame zone. Within the combustion chamber, the reflection of light off the solid metal chamber walls may be an issue. To mitigate the effect of such reflection, the shortest possible wavelength should be chosen because the reflectivity of metal decreases at shorter wavelengths (see textbooks of radiative heat transfer, Ref. 24, for example).

The suitable exposure time for application to experimental emission images also should be noted. In the experiment by Ivancic and Mayer [8], the length scales of OH* emission were successfully evaluated with the exposure time of 100 ns under an extremely high Reynolds number ($Re = 10^6$). In addition, they performed numerical simulations and evaluated the smallest Kolmogorov time scales to be approximately 1 μs near the injector exit. The exposure time of 1/10 of the smallest turbulent time scales gives instantaneous emission images, and the evaluation of emission length scales has been successfully applied in high-pressure rocket combustors at high Reynolds numbers.

While the correlation between the OH* emission length scales and the turbulent length scales has not been clarified in the present study, OH* emissions are also expected to be used for evaluating turbulent length scales, as shown in Ivancic and Mayer's works [7,8]. In addition, the correlation between the OH* emission length scales and the turbulent length scales will be investigated in the future.

5. Conclusions

The correlation between optical emissions and turbulent length scale for a coaxial jet diffusion

flame is investigated in this article. The characteristics of optical emission from a one-dimensional opposed-flow diffusion flame are examined by the radiative transfer calculation of a one-dimensional flame profile. The emission intensities from a flame decrease as the flame becomes thinner, i.e. as the strain rate on the flame increases. The dependence of emission intensity on flame thickness shows a linear trend for the flame thicknesses larger than 1 mm. The emission intensities at wavelengths shorter than 4 μm decrease rapidly for flame thicknesses smaller than 1 mm due to the reduction in the flame temperature. A resolution convergence study regarding wavelength shows that a resolution of 10^{-4} μm gives sufficiently accurate solutions under the optically thin condition of the present flame.

To generate time series data for turbulent diffusion flame, an LES is conducted for a cylindrical combustor with a single coaxial injector element. The integral length scales of velocity and temperature are obtained along the line of maximum velocity of the turbulent annular H_2 jet by two-point correlation methods. H_2O emission images are then simulated by solving the RTE on the LES flowfield. The simulated emission images show that the distributions of emission intensities in the images duplicate patterns on the flame surface. The length scales of visible structures in the emission images are determined by the two point correlation of emission intensity. Length scales obtained from emission images agree well with the integral length scale of temperature, and are also close to those of radial velocity components. The validity of estimating length scale from emission images is explained by the comparison of distributions of temperature and emission intensity. Emission intensity distributions on the symmetry line of emission images simply correspond to the flame thickness distribution, and the spatial correlation of emission intensity is linked with that of temperature. As a consequence, the integral length scale of temperature can be extracted from H_2O emission images. The estimation of integral length scales from actual experimental emission images may also be possible, and a database for integral length scale is valuable for the CFD validation of

cryogenic combustion.

Acknowledgements

This work was supported by a Grant-in-Aid for Young Scientists (B) from Japan Society for the Promotion of Science [Grant 22760162].

References

- [1] W. Mayer, H. Tamura, *Journal of Propulsion and Power* 12 (1996) 1137-1147.
- [2] G. Herding, R. Snyder, C. Rolon, S. Candel, *Journal of Propulsion and Power* 14 (1998) 146-151.
- [3] D. Kendrick, G. Herding, P. Scouflaire, C. Rolon, S. Candel, *Combustion and Flame* 118 (1999) 327-339.
- [4] A. Tripathi, M. Juniper, P. Scouflaire, C. Rolon, D. Durox, S. Candel, AIAA-1999-2490 (1999) 1-10.
- [5] M. Juniper, A. Tripathi, P. Scouflaire, C. Rolon, S. Candel, *Proceedings of the Combustion Institute* 28 (2000) 1103-1109.
- [6] M. Juniper, Doctoral thesis, Ecole Centrale Paris, Chatenay-Malabry, 2001.
- [7] B. Ivancic, W. Mayer, G. Krülle, D. Brüggemann, AIAA-1999-2211 (1999) 1-11.
- [8] B. Ivancic, W. Mayer, *Journal of Propulsion and Power* 18 (2002) 247-253.
- [9] E. A. Luke, P. Cinnella, *Computers and Fluids* 36 (2007) 1547-1566.
- [10] T. Schmitt, Y. Méry, M. Boileau, S. Candel, *Proceedings of the Combustion Institute* 33 (2011) 1383-1390.
- [11] M. Poschner, M. Pfitzner, AIAA-2010-1144 (2010) 1-12.
- [12] TNF Workshop web site, <http://www.ca.sandia.gov/TNF>, Sandia National Laboratories 2013.
- [13] G. Singla, P. Scouflaire, C. Rolon, S. Candel, *Combustion and Flame* 144 (2006) 151-169.

- [14] A. Vaidyanathan, J. Gustavsson, C. Segal, *Journal of Propulsion and Power* 25 (2009) 864-874.
- [15] G. Singla, P. Scouflaire, C. Rolon, S. Candel, L. Vingert, *Journal of Propulsion and Power* 23 (2007) 593-602.
- [16] M. S. Liu, *Journal of Computational Physics* 214 (2006) 137-170.
- [17] G. S. Jiang, C.-W. Shu, *Journal of Computational Physics* 126 (1996) 202–228.
- [18] B. Thornber, A. Mosedale, D. Drikakis, D. Youngs, R. J. R. Williams, *Journal of Computational Physics* 227 (2008) 4873-4894.
- [19] J. Li, Z. Zhao, A. Kazakov, F. L. Dryer, *International Journal of Chemical Kinetics* 36 (2004) 1-10.
- [20] B. J. McBride, M. J. Zehe, S. Gordon, NASA Technical Report TP-2002-211556, 2002.
- [21] R. J. Kee, G. Dixon-Lewis, J. Warnatz, M. E. Coltrin, J. A. Miller, Sandia National Laboratories Report No. SAND86-8246, 1986.
- [22] R. B. Bird, W. E. Stewart, E. N. Lightfoot, *Transport Phenomena*, John Wiley and Sons, New York, p. 258.
- [23] J. S. Mathur, P. K. Tondon, S. C. Saxena, *Molecular Physics* 12 (1967) 569-579.
- [24] M. F. Modest, *Radiative Heat Transfer*, Academic Press, New York, 2003.
- [25] T. Koike, K. Morinaga, *Bull. Chem. Soc. Jpn.* 55 (1982) 52-54.
- [26] Y. Hidaka, S. Takahashi, H. Kawano, M. Suga, W. C. Gardiner, *Int. J. Chem. Phys.* 86 (1982) 1429-1433.
- [27] G. Smith, C. Park, J. Luque, *Combustion and Flame* 140 (2005) 385-389.
- [28] J. M. Hall, E. L. Petersen, *Int. J. Chem. Kinet.* 38 (2006) 714-724.
- [29] T. Kathrotia, M. Fikri, M. Bozkurt, M. Hartmann, U. Ridel, C. Schulz, *Combustion and Flame* 157 (2010) 1261-1273.
- [30] L. S. Rothman, I. E. Gordon, R. J. Barber, H. Dothe, R. R. Gamache, A. Goldman, V. I.

Perevalov, S. A. Tashkun, J. Tennyson, *Journal of Quantitative Spectroscopy and Radiative Transfer* 111 (2010) 2139-2150.

[31] CHEMKIN Collection, Release 4.1, Reaction Design, Inc.: San Diego, CA 92121, USA.

[32] C. J. Sung, J. B. Liu, C. K. Law, *Combustion and Flame* 102 (1995) 481-492.

[33] T. M. Brown, M. A. Tanoff, R. J. Osborne, R. W. Pitz, M. D. Smooke, *Combustion Science and Technology* 129 (1997) 71-88.

[34] G. Ribert, N. Zong, V. Yang, L. Pons, N. Darabiha, S. Candel, *Combustion and Flame* 154 (2008) 319-330.

[35] S. A. Schumaker, J. F. Driscoll, *Proceedings of the Combustion Institute* 32 (2009) 1655-1662.

[36] K. M. Tacina, W. J. A. Dahm, *Journal of Fluid Mechanics* 415 (2000) 23-44.

[37] S. A. Schumaker, Ph.D. Thesis, University of Michigan, 2009.

[38] W. C. Gardiner, JR., Y. Hidaka, T. Tanzawa, *Combustion and Flame* 40 (1981) 213-219.

List of Tables

- 1 H₂/O₂ reaction mechanism used in present study. Reaction rate coefficients are expressed as $k = AT^n \exp(-E/RT)$. All reaction rate constants have been taken from Li et al. [19]
- 2 Injection conditions for LES of coaxial jet diffusion flame

List of Figures

- 1 Example of absorption coefficients of H₂O computed using the HITEMP 2010 database for typical flame properties of H₂/O₂ diffusion flame (T = 3040 K, P = 100 kPa, 55.84% of H₂O by mole).
- 2 Schematic diagram of combustor considered in present study, showing (a) dimensions of cylindrical combustor equipped with single shear coaxial injector, (b) geometry of coaxial injector element, and (c) details of computational domain.
- 3 Schematic diagram of present numerical setup for radiative transfer calculations. The solid lines with arrows indicate the rays along which light passes through the flame and onto the image plane of the CCD camera.
- 4 Profiles of temperature and number density of H₂O for one-dimensional opposed-flow diffusion flame. Calculations are performed at $a = 280, 820, 2327, 7000, \text{ and } 18705 \text{ s}^{-1}$. The

fuel boundary is on the positive side, and the oxidizer boundary is on the negative side of the one-dimensional ordinate.

- 5 H₂O emission intensities from one-dimensional H₂/O₂ diffusion flame as a function of inverse of flame thickness with different wavelength ranges. Emission intensities are computed by solving the RTE along the one-dimensional flame profiles. The global strain rate on the flame is varied between 3.36 and $1.1 \times 10^5 \text{ s}^{-1}$, resulting in flame thicknesses ranging from 35 to 0.147 mm.
- 6 H₂O emission intensities from one-dimensional H₂/O₂ diffusion flame as a function of number of wavelength points with different wavelength ranges. The computed intensity for each number of wavelength points is normalized against that of 10^6 wavelength points. Calculations are performed for $a = 280 \text{ s}^{-1}$ by varying the number of wavelength point from 10^2 to 10^6 .
- 7 Instantaneous contours of (a) temperature (in K) and (b) vorticity magnitude (in s^{-1}) in the X - Y plane ($Z = 0 \text{ mm}$) at $t = 40 \text{ ms}$.
- 8 Three-dimensional structures of flame and vortices for H₂/O₂ coaxial jet flame. Iso-surfaces of (a) temperature ($T = 1000 \text{ K}$) and (b) second invariant of velocity gradient tensor ($Q = 2(U_{H_2}/D_o)^2$) colored by the streamwise vorticity ($-2(U_{H_2}/D_o) < \omega_x < 2(U_{H_2}/D_o)$) are shown.
- 9 Resolved kinetic energy spectrum for present LES. (a) Power spectrum of radial velocity fluctuations at three different probe locations. (b) Probe locations at which the time-series data

are collected are shown with vorticity magnitude.

- 10 Comparison of stoichiometric mixing lengths between present LESs and experimental data of Schumaker and Driscoll [35]. The Stoichiometric mixing lengths are normalized against D_i and plotted against the scaling parameter with the effective momentum flux ratio ($M_{eff} = (\rho_{H2})_{eff} U_{H2}^2 / (\rho_{O2} U_{O2}^2)$) and the mole fraction of the inner jet fluid in a stoichiometric mixture ($X_s = 0.34$). The dashed line represents the scaling law for coaxial jet flames [35]. The present LESs are performed on baseline mesh (baseline) and coarse mesh (coarse). Velocity fluctuations are added to the inlet velocity for the case with the coarse mesh (coarse + v').
- 11 Radial location of the maximum-velocity line fitted by Eq. (12) with time-averaged axial velocity field (in m/s). The integral length scales of the present LES flowfield are computed along the maximum-velocity line.
- 12 Integral length scales of radial, circumferential, and axial velocity components (U_r, U_θ, U_x) and temperature obtained from LES flowfield data. Results are shown for (a) baseline mesh, (b) coarse mesh, and (c) coarse mesh with velocity fluctuations. The solid lines show the results obtained with spatial increments in the $+\Delta X$ direction, and the dashed lines show those with spatial increments in the $-\Delta X$ direction.
- 13 Simulated H₂O emission images at $t = 40$ ms. (top) Corresponding flame shapes from the iso-surfaces of temperature for $T = 1000$ and 2500 K. (bottom) Emission images computed considering six different wavelength ranges.

- 14 Examples of correlation functions of emission intensity computed according to Eq.(16) at $X = 20, 30,$ and 40 mm for wavelengths of $1\text{--}2\ \mu\text{m}$. The emission length scales are defined as the spatial increment ΔX at which $K(\Delta X) = 0.5$.
- 15 Length scales obtained from simulated emission images with different wavelength ranges. The solid black lines are the integral length scales of the velocity components and temperature evaluated from the LES flowfield data (same results with Fig. 12). Results are shown for (a) baseline mesh, (b) coarse mesh, and (c) coarse mesh with velocity fluctuations.
- 16 Computed refraction angles due to density gradient in H_2/O_2 coaxial jet flame. Refraction of light is evaluated along the rays on the $Y = 0$ mm plane using 1,000 time series data of the LES flowfield. Instantaneous data are indicated on the scatter plot by the gray symbols. The solid line shows time-averaged data at each X location.
- 17 Cross section of instantaneous temperature field at the $Y = 0$ mm plane and the corresponding emission intensity distributions with different wavelength ranges. Radiative transfer calculations are conducted in the $+Z$ direction from the top to bottom of the temperature cross section. The emission intensity is normalized by its peak value for each wavelength range.

Table 1 H₂/O₂ reaction mechanism used in present study. Reaction rate coefficients are expressed as

$k = AT^n \exp(-E/RT)$. All reaction rate constants have been taken from Li et al. [19]

No.	Reaction	A (cm mol s)	n	E (J mol ⁻¹)	
1	H+O ₂ =O+OH	3.547×10^{15}	-0.406	1.6599×10^4	
2	O+H ₂ =H+OH	0.508×10^5	2.67	0.629×10^4	
3	H ₂ +OH=H ₂ O+H	0.216×10^9	1.51	0.343×10^4	
4	O+H ₂ O=OH+OH	2.970×10^6	2.02	1.340×10^4	
5	H ₂ +M=H+H+M ^a	4.577×10^{19}	-1.40	1.0438×10^5	
6	O+O+M=O ₂ +M ^a	6.165×10^{15}	-0.50	0	
7	O+H+M=OH+M ^a	4.714×10^{18}	-1.00	0	
8	H+OH+M=H ₂ O+M ^a	3.800×10^{22}	-2.00	0	
9	H+O ₂ +M=HO ₂ +M ^b	k ₀	6.366×10^{20}	-1.72	5.248×10^2
		k _∞	1.475×10^{12}	0.60	0
10	HO ₂ +H=H ₂ +O ₂	1.660×10^{13}	0.00	0.823×10^3	
11	HO ₂ +H=OH+OH	7.079×10^{13}	0.00	2.950×10^2	
12	HO ₂ +O=O ₂ +OH	0.325×10^{14}	0.00	0	
13	HO ₂ +OH=H ₂ O+O ₂	2.890×10^{13}	0.00	-4.970×10^2	

^aEfficiency factors are: $\epsilon_{H_2}=2.5$, $\epsilon_{H_2O}=12.0$.

^bEfficiency factors are: $\epsilon_{H_2}=2.0$, $\epsilon_{H_2}=0.78$, $\epsilon_{H_2O}=11.0$. Troe parameter is: $F_c=0.8$.

Table 2 Injection conditions for LES of coaxial jet diffusion flame

	H ₂	O ₂
Mass flow rate [g/s]	0.473	2.419
Temperature [K]	300	300
Density [kg/m ³]	8.082×10^{-2}	1.283
Velocity at injector exit [m/s]	270	100
Reynolds number* [-]	1.916×10^4	3.039×10^4
Mach number [-]	0.2048	0.3033
O/F		5.11
Chamber pressure [kPa]		100

*Based on the outer diameter H₂ annuls and the inner diameter of O₂ tube.

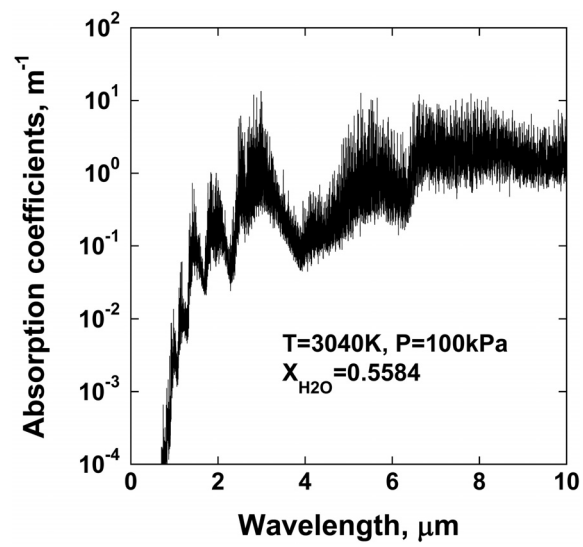
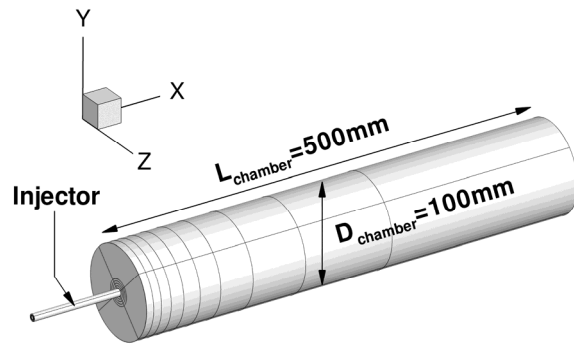
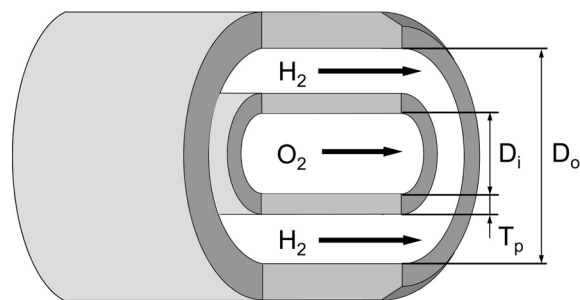


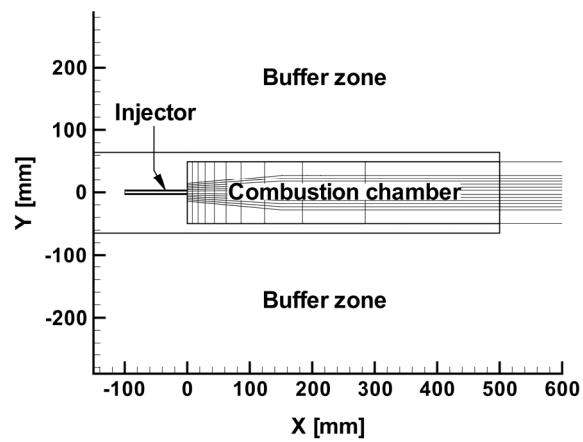
Fig. 1.



(a)



(b)



(c)

Fig. 2.

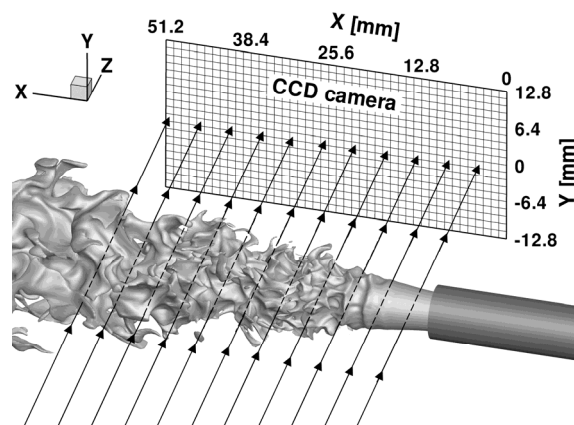
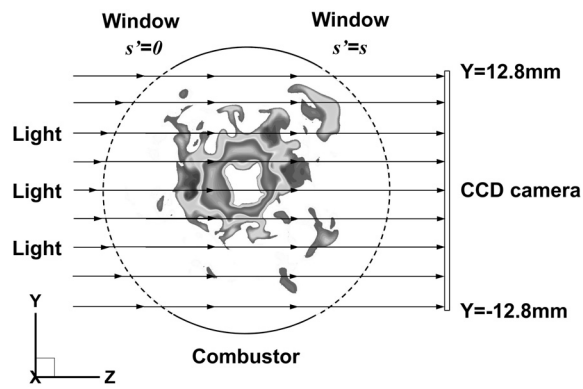
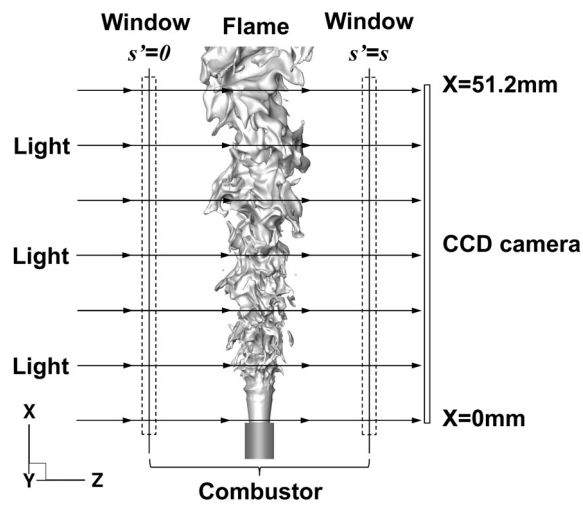


Fig. 3.

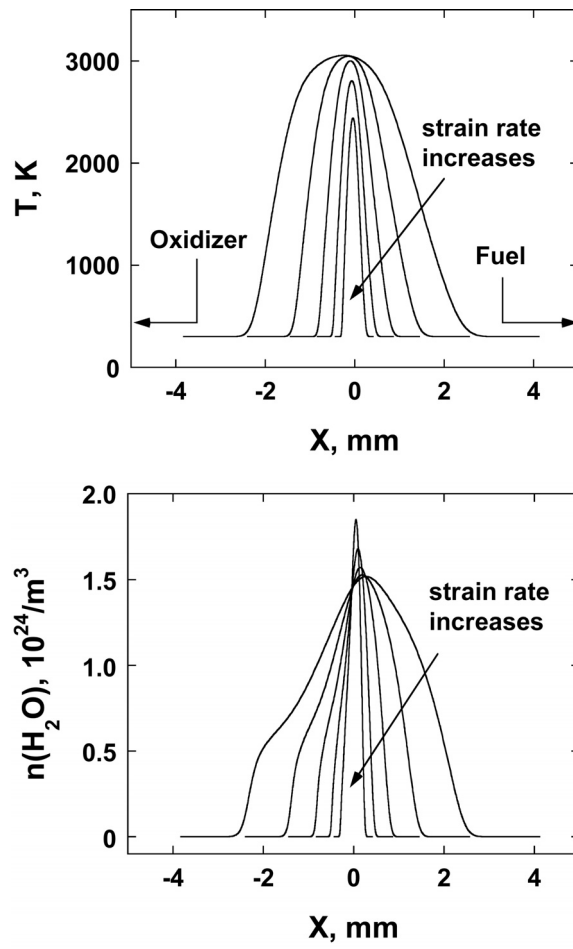


Fig. 4.

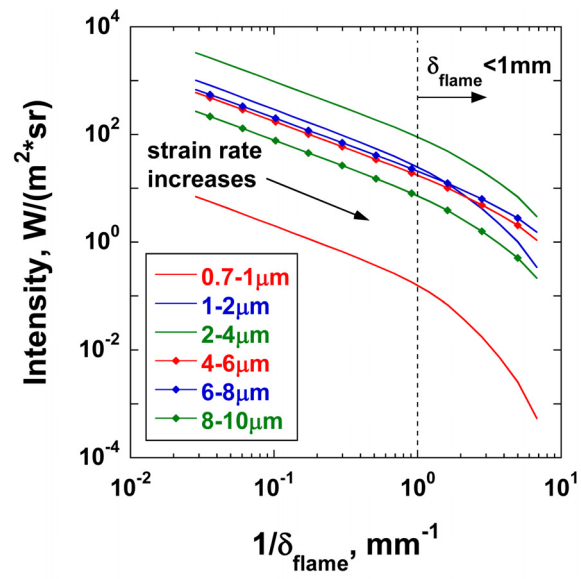


Fig. 5.

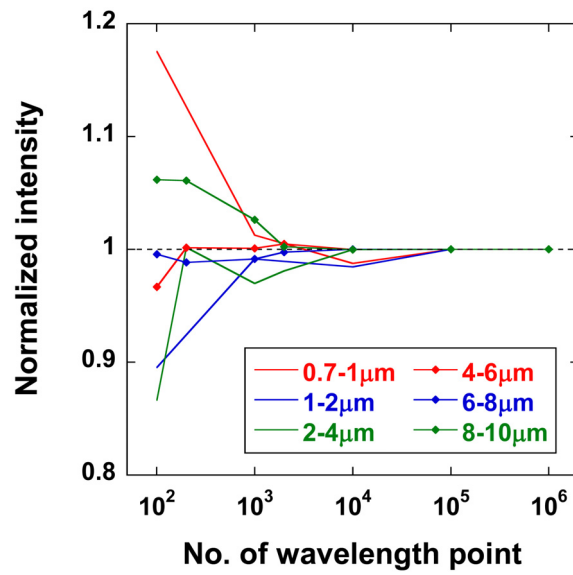
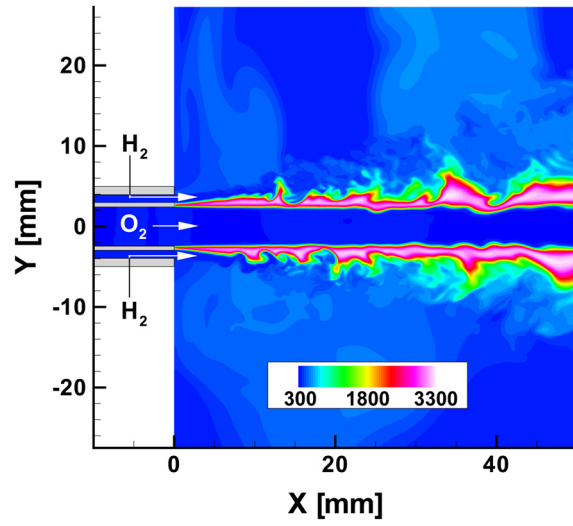
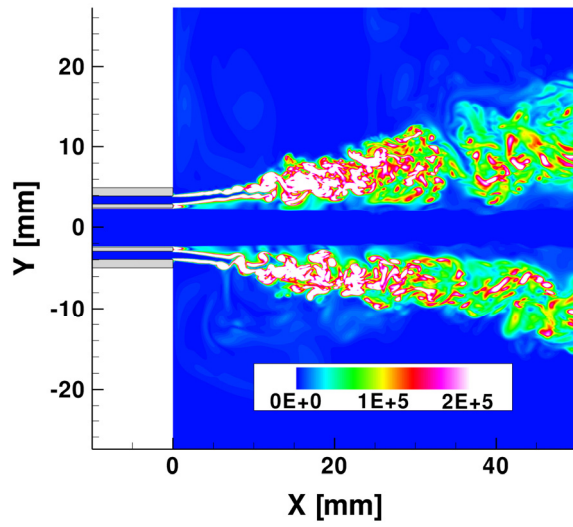


Fig. 6.

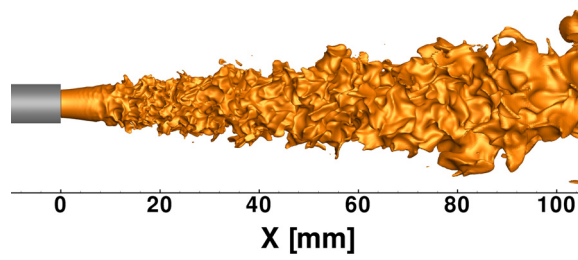


(a)

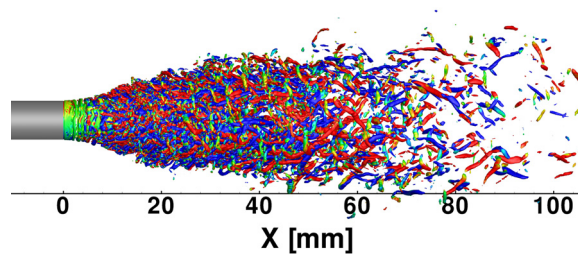


(b)

Fig. 7.

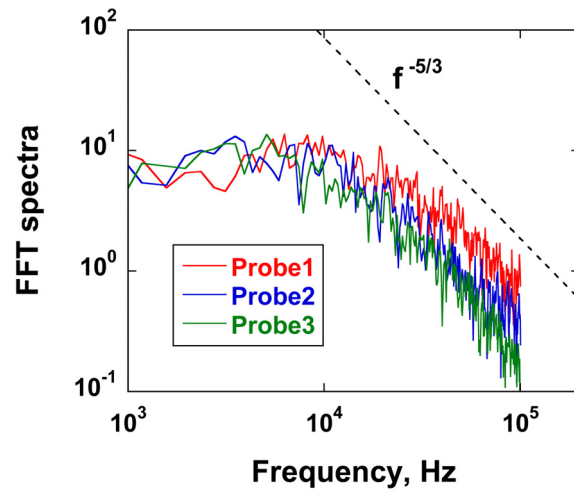


(a)

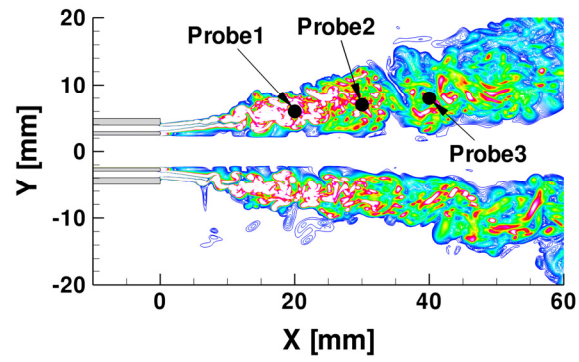


(b)

Fig. 8.



(a)



(b)

Fig. 9.

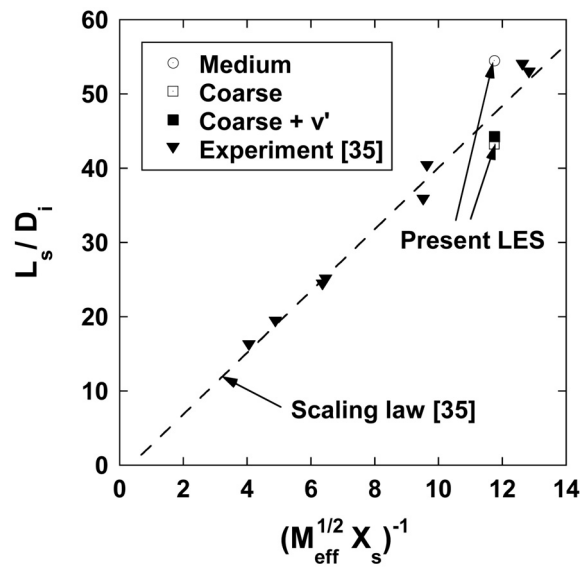


Fig. 10.

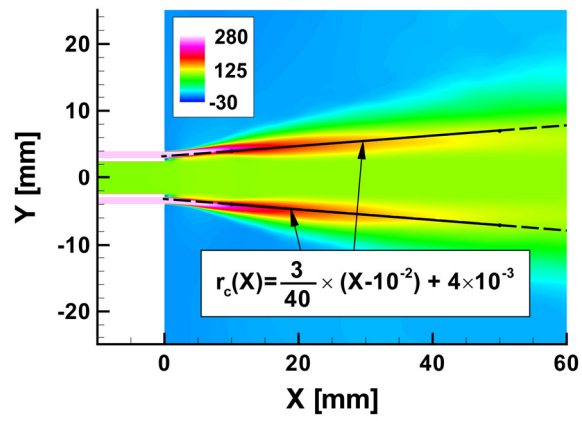


Fig. 11.

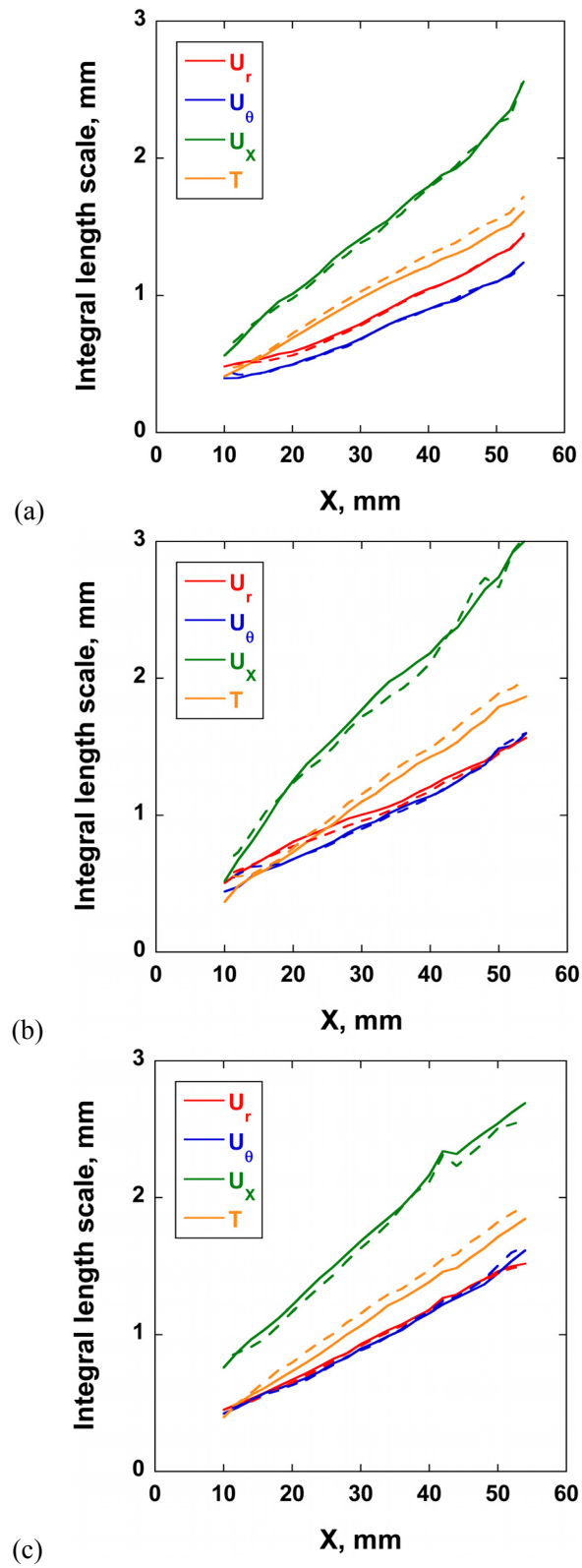


Fig. 12.

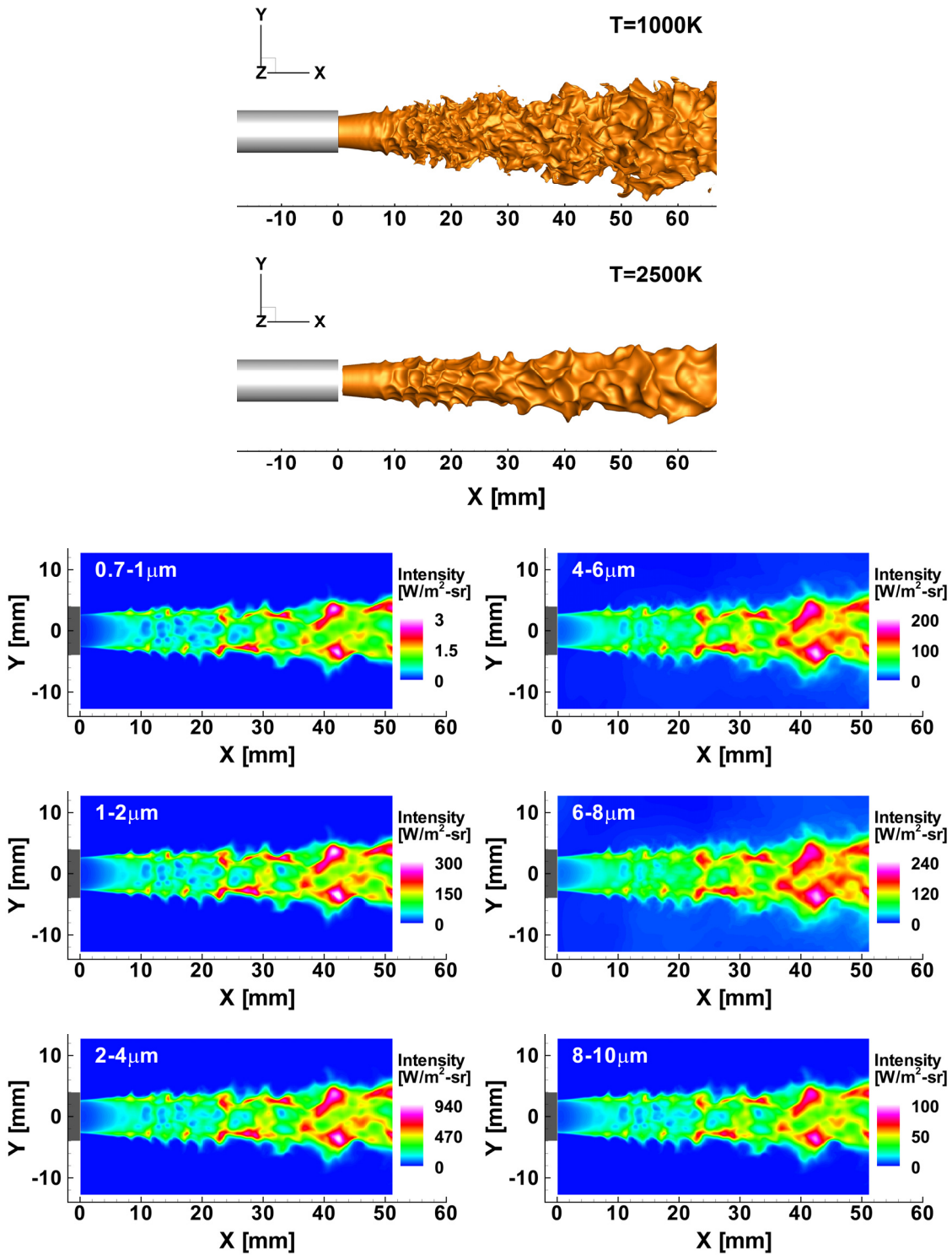


Fig. 13.

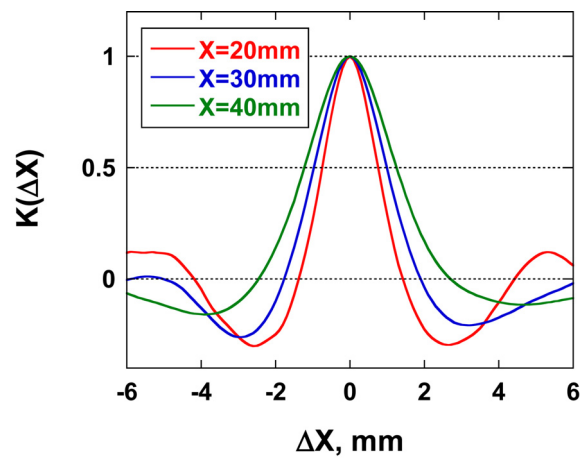


Fig. 14.

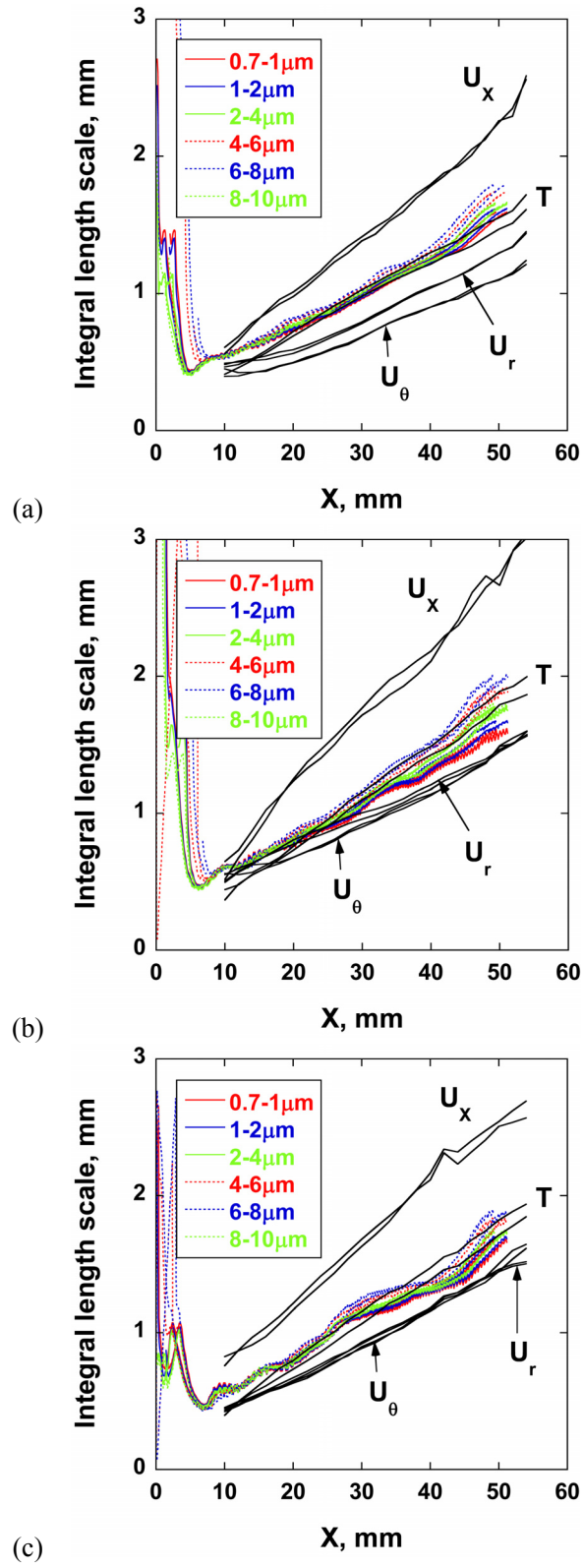


Fig. 15.

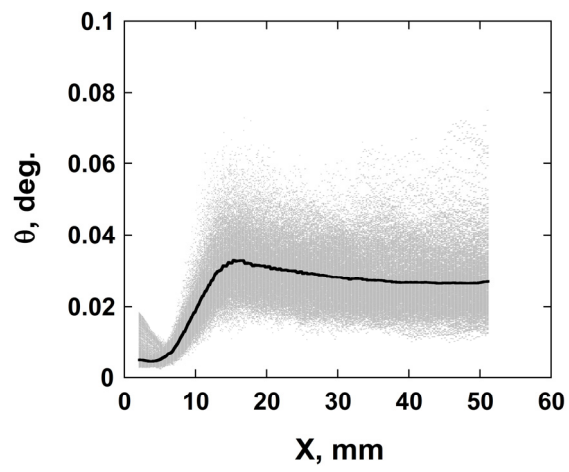


Fig. 16.

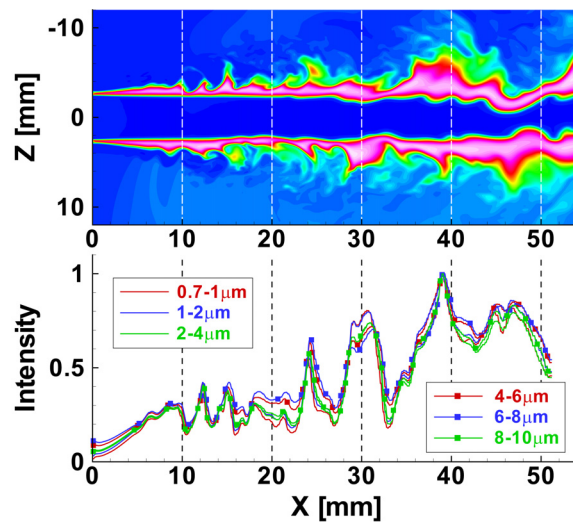


Fig. 17.